Materials & Design 229 (2023) 111864

Contents lists available at ScienceDirect

Materials & Design

journal homepage: www.elsevier.com/locate/matdes

Microstructure control and property switching in stress-free van der Waals epitaxial VO_2 films on mica

Erik Ekström [a], Simon Hurand [b], Arnaud le Febvrier [a], Anna Elsukova [a], Per O.Å. Persson [a], Biplab Paul [a], Fredrik Eriksson [a], Geetu Sharma [c], Oleksandr Voznyy [d], Davide G. Sangiovanni [a], Ganpati Ramanath [a,c,*], Per Eklund [a,*]

[a] Thin Film Physics Division, Department of Physics, Chemistry, and Biology (IFM), Linköping University, SE-58183 Linköping, Sweden
[b] Institut Pprime, Département de Physique et Mécanique des Matériaux, UPR 3346, CNRS-Université de Poitiers-ENSMA, 11 Boulevard Marie et Pierre Curie, - TSA 41123, 86073 Poitiers Cedex 9, France
[c] Rensselaer Polytechnic Institute, Department of Materials Science and Engineering, Troy, NY 12180, USA
[d] University of Toronto Scarborough, Department of Physical and Environmental Sciences, Scarborough M1C 1A4, ON, Canada

HIGHLIGHTS

- van der Waals epitaxy (VDWE) of non-layered stress-free VO_2 films on mica.
- Epitaxy with weak film-substrate bonding and complete interfacial stress relaxation.
- Narrow domain-size-sensitive electrical-conductivity-temperature hysteresis.
- Ab initio studies indicate that VDWE involves surface potassium atoms in the mica.

GRAPHICAL ABSTRACT

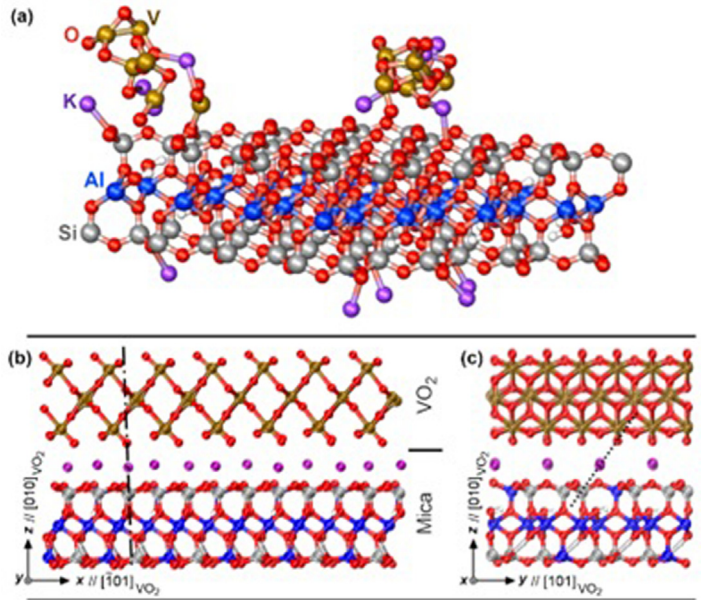

ARTICLE INFO

Article history:
Received 12 September 2022
Revised 20 March 2023

ABSTRACT

Realizing stress-free inorganic epitaxial films on weakly bonding substrates is of importance for applications that require film transfer onto surfaces that do not seed epitaxy. Film-substrate bonding is usually weakened by harnessing natural van der Waals layers (e.g., graphene) on substrate surfaces, but this is

* Corresponding authors at: Thin Film Physics Division, Department of Physics, Chemistry, and Biology (IFM), Linköping University, SE- 58183 Linköping, Sweden (P. Eklund) and Rensselaer Polytechnic Institute, Department of Materials Science and Engineering, Troy, NY 12180, USA (G. Ramanath).
E-mail addresses: ganapr@rpi.edu (G. Ramanath), per.eklund@liu.se (P. Eklund).

https://doi.org/10.1016/j.matdes.2023.111864

Accepted 22 March 2023
Available online 26 March 2023

Keywords:
vad der Waals epitaxy
Thin films
X-ray diffraction
Electronic properties

difficult to achieve in non-layered materials. Here, we demonstrate van der Waals epitaxy of stress-free films of a non-layered material VO_2 on mica. The films exhibit out-of-plane 010 texture with three in-plane orientations inherited from the crystallographic domains of the substrate. The lattice parameters are invariant with film thickness, indicating weak film-substrate bonding and complete interfacial stress relaxation. The out-of-plane domain size scales monotonically with film thickness, but the in-plane domain size exhibits a minimum, indicating that the nucleation of large in-plane domains supports subsequent island growth. Complementary *ab initio* investigations suggest that VO_2 nucleation and van der Waals epitaxy involves subtle polarization effects around, and the active participation of, surface potassium atoms on the mica surface. The VO_2 films show a narrow domain-size-sensitive electrical-conductivity-temperature hysteresis. These results offer promise for tuning the properties of stress-free van der Waals epitaxial films of non-layered materials such as VO_2 through microstructure control.

1. Introduction

There is a widespread interest in integrating epitaxial thin films of inorganic materials with organic and amorphous substrates for a variety of applications in energy and electronics. Conventional thin-film epitaxial growth [1] involves a strongly bonded film-substrate interface, which is unsuited for applications requiring free-standing films or those requiring transfer on to substrates that do not support epitaxy. Epitaxy with diminished film-substrate bonding is generically referred to as van der Waals epitaxy (VDWE) [2–3] and involves the use of surface-terminated substrates, [4] layered substrates, [5] or a two-dimensional buffer layer with no dangling bonds. [6] VDWE has been demonstrated in many organic [7] and inorganic systems. [3] On one extreme, films grown by pure VDWE are expected to be completely stress-free, regardless of lattice mismatch, due to the absence of interfacial strain, and exhibit both in-plane and out-of-plane textures. All these three attributes have been demonstrated in layered 2D materials, e.g., graphene [8–9], transition metal chalcogenides [10–12], nitrides [13] and oxides [14]. However, there are also reports of cases involving only partial strain relaxation, in particular cases where the structure, bond symmetry, and lattice parameters are similar, and can be used for strain engineering in heterostructures with mixed bonding between different layers. [15] Those cases are therefore somewhat reminiscent of conventional epitaxy where stronger bonds are involved in addition to van der Waals bonding. This more complex form of VDWE is thus distinct from the case of pure VDWE, with complete strain relaxation without interfacial misfit dislocations. In the present work, we demonstrate pure VDWE of a non-layered material with all three key characteristics, namely, full interfacial strain relaxation, and both in-plane and out-of-plane textures.

VO_2 is a non-layered polymorphic material with an insulator-to-metal phase transition [16–20] that renders it attractive for thermochromic [21–24] and electronic applications [25–27]. Recent works have suggested VDWE of monoclinic VO_2 on mica [25,28–30] and boron nitride [31], but without adequate or sufficient evidence of stress-relaxation. For example, VDWE has been claimed based solely on film texture either without measuring film strain [25], or by suggesting weak film-substrate bonding despite clear contrary evidence of significant interfacial strain [29]. VDWE has also been inferred in VO_2 nanorods [31] on boron nitride based on narrow metal-to-insulator transition temperature ranges similar to that in stress-free films, without evidence of out-of-plane crystallographic orientation. Establishing all three conditions is essential to definitively infer pure VDWE in non-layered materials such as VO_2, where strong film-substrate bonding cannot be automatically ruled out.

Our VDWE VO_2 films are stress-free irrespective of film thickness and exhibit out-of-plane stacking of basal planes in three in-plane domains corresponding to the threefold variants of mica substrate crystals. The results indicate that epitaxy is initiated by the nucleation of large in-plane domains that support subsequent island growth. Results of *ab initio* calculations reveal subtle chemical and polarization effects that induce VDWE of VO_2 on mica. The electrical conductivity switching hysteresis associated with the metal-insulator transition in VO_2 scales with the crystal domain, indicating possibilities of property tuning through microstructural control of VDWE VO_2 films. These findings indicate the necessity of providing evidence of all three requirements for claiming pure VDWE of non-layered materials and should be applicable to a variety of materials systems and properties.

2. Experimental and theoretical methods

2.1. Film growth

VO_2 thin films were deposited with thicknesses between 17 nm $\leq t_{film} \leq$ 180 nm by reactive pulsed magnetron sputter deposition on muscovite mica (001) substrates in a 2×10^{-8} Torr (2.7×10^{-6} Pa) base-pressure chamber described in detail elsewhere [50]. Immediately prior to deposition, a fresh surface of the mica substrate was exposed by peeling off the top layer by tape. During sputter deposition, the magnetron was operated at 160 W at a 50 kHz pulsing frequency and a reverse voltage that was 10% of the driving voltage for 2 s, resulting in a 90 % duty cycle. The substrate temperature was maintained at 400 °C, and a plasma struck with a 11.5 % O_2-88.5%Ar gas mixture resulted in a 2.3 mTorr (0.31 Pa) pressure during deposition. The film thickness was controlled by adjusting the deposition time between 5 and 60 min.

2.2. Microstructural characterization

Scanning electron microscopy (SEM) was used to observe the morphology of the films using a LEO Gemini 1550 Zeiss instrument operated at 5 kV. For transmission electron microscopy (TEM), please refer to the Supplementary Information.

A large set of X-ray diffraction (XRD) measurements were carried out to characterize various structural features of the epitaxial films. All these experiments used incident Cu Kα X-rays obtained from sources operated at 45 kV and 40 mA. Symmetric θ-2θ scans were acquired from the as-deposited films using a X'pert-Pro powder diffractometer with a X'celerator detector operated in scanning line mode with a 2.122° active length. Pole figure measurements were carried out by using a point-focus configuration together with cross slits, a parallel plate collimator, and an Xe-gas-filled proportional counter detector. We used X-ray reflectivity (XRR) measurements for film thickness determination, and reciprocal space mapping (RSM) and φ scans for quantitatively understanding the texture. These measurements were carried out using a PANa-

lytical Empyrean diffractometer equipped with a hybrid monochromator 2-bounce Ge(220) crystal in the incident beam path and a triple-axis Ge (220) 3-bounce symmetrical analyser together with a PIXcel-3D detector. The thickness of the thickest film weas determined by extrapolating the deposition time and thickness data from the other three films. t_{film} were determined to 17 nm, 26 nm, 62 nm, and 180 nm using XRR. Misalignments in the q_x position of the asymmetrical reflections were corrected by the q_x position of the symmetrical reflections. Additionally, mosaicity broadening in Δq_x where not taken into account and a slightly larger lateral correlation length is expected.

2.3. Temperature-dependent electrical-property measurements

The conductivity of the thin films was measured in a four-probe van der Pauw configuration with a Keithley 2401 multimeter. The sample was located inside the closed chamber of a Linkam heat cell, providing a temperature stability of less than 0.01 °C, and the temperature was swept linearly from 30 °C to 90 °C and then backwards in 12 h of time to avoid any temperature offset between the thermometer and the sample.

Joule heating of the sample by the input current needs to be carefully avoided in order to correctly measure the insulator-to-metal transition versus temperature: as the conductivity endures a 3 order of magnitude change through the transition, the built-in autorange of the multimeter cannot be used as it happened to result in an excessive current (>100 mA) in the high-temperature (metallic) phase. To do so, at each measured temperature, a very low input current of 10 μA was first applied in order to estimate the order of magnitude of the resistance. Then an adequate current was applied depending on the resistance range, which is low enough to avoid any Joule heating of the sample, but high enough to provide a noiseless measurement of the resistance: from 10 μA for the insulating phase ($R \sim 20$ kΩ) to 1 mA for the metallic phase ($R \sim 3$ Ω). By doing do, the Joule heating power is kept below ~3 mW in the metallic phase, which is way smaller than the heating power of the temperature cell, and it was checked that a measurement with even lower current provides exactly the same temperature dependence of the conductivity.

2.4. Ab initio methods

2.4.1. Molecular dynamics

Ab initio molecular dynamics simulations [51] (AIMD) were carried out using CP2K software suite and Quickstep module for density functional theory (DFT). We used Double-zeta plus polarization basis sets optimized for molecules (DZVP-MOLPOT) [52], Goedecker-Teter-Hutter pseudopotentials [53], and PBE functional [54] were used throughout. A 21 Å x 21 Å unit cell with 1 mica layer and 20 Å of vacuum between layers was used, where 32 VO_2 molecules were randomly placed and were allowed to fully relax and interact at 600 K for 4 ps with a 4 fs timestep, while the mica atoms remained fixed.

2.4.2. Density functional theory (DFT) calculations

Electron-transfer maps at VO_2-mica interfaces with 50% and 100% potassium coverage were obtained by subtracting the self-consistent electron density of isolated VO_2, and mica, from that of the VO_2/mica slab through DFT conjugate-gradient energy minimization. We used the VASP code with projector augmented-wave pseudopotentials [55], and combined the generalized-gradient approximation of Perdew-Burke-Ernzerhof for electronic exchange and correlation [54] with the rev-vdW-DF2 description of nonlocal correlation energies associated with long-range van der Waals interactions [56]. Since the 3d states are strongly localized in vanadium, we employed on-site Coulomb and exchange interactions of 4.2 eV and 0.8 eV, respectively, and corrected for double-counting [57].

The atomic positions for muscovite mica and monoclinic VO_2 were taken from Materials Project (mp-1200795 and mp-1102963). DFT structural relaxation was carried out to achieve 10^{-5} eV/supercell accuracy and atomic forces smaller than 10^{-2} eV $Å^{-1}$. All calculations were based on Γ-point sampling of the reciprocal space and 400 eV cutoff energy for the planewave basis set. Full structural optimization of the VO_2-mica interface was achieved as follows. First, we relaxed a 30.810 Å x 17.918 Å mica surface containing 24 K, 72 Al, 72 Si, 48 H and 288 O atoms to achieve negligible stresses (<0.2 GPa). Then a VO_2 film (rotated to make a VO_2/mica interface consistent with our experimental observations) comprised of 126 V and 336 O atoms was relaxed on top of the mica substrate (966 atoms in total). A 17-Å-long vacuum region separates VO_2/mica slab replicas along the surface normal direction. Electrostatic corrections were applied to cancel spurious dipole/dipole interactions among vertical supercell replicas.

3. Results

SEM micrographs (Fig. 1) from the as-deposited VO_2 films show polycrystalline microstructures with monomodal grain size distributions (see supplementary Fig. S1). The thinnest film, i.e., t_{film} = 17-nm (Fig. 1a), has an average lateral grain size of 23 nm, whereas thicker films with $26 \leq t_{film} \leq 180$ nm (Fig. 1b-d) have larger average grain sizes of 55 nm ± 10 nm that do not scale with film thickness. The contrast differences observed in the SEM images (Fig. 1a-d) suggest that the thinner films are flatter than the thicker films.

X-ray diffractograms (see Fig. 2a) showing strong 020 and 040 reflections from VO_2 films indicate a strong out-of-plane 010 basal plane texture. Besides these and the 00 *l* mica substrate reflections, no other Bragg reflections were detectable. VO_2 deposition on amorphous SiO_2 under similar conditions do not result in such 010 texture (see supplementary Fig. S2), indicating that this texture is induced by the mica substrate. The VO_2 0 *k*0 peak intensities increase monotonically with t_{film}, but the 0 *k*0 peak positions are unchanged within experimental uncertainties for 17 nm $\leq t_{film} \leq$ 180 nm. The out-of-plane lattice parameter *b* = 0.452 ± 0.001 n m is within 0.3% of that reported [32] for unstrained VO_2 (see supplementary Fig. S3) indicating that the VO_2 films are not constrained by interfacial strain with the substrate.

Extensive attempts to carry out transmission electron microscopy (TEM) were unsuccessful due the delamination of VO_2 from the mica substrates and/or formation of V_2O_3 and carbon-vanadium compound during sample preparation by either focused ion beam milling or mechanical polishing. This outcome was not entirely unexpected, and indeed confirms weak film-substrate bonding characteristic of VDWE. Please refer to the Supplementary Information (Fig S4 and corresponding text) for more details.

All the as-deposited VO_2 films exhibit in-plane texture as well. X-ray pole figures of the 031 reflection ($2\theta = 65.1°$) show a sextet of angularly equidistant peaks at $\Delta\phi = 60°$, $\psi = 20°$ (see Fig. 3a-d), also observed in ϕ scan as shown in supplementary Fig. S5. This sextet arises from four 130- and 031-type reflections from monoclinic VO_2, where the 130 and 031 peaks are close ($\Delta 2\theta \approx 0.5°$). In particular, the hexagonal pattern of the 130-031 doublets is obtained from three-fold rotations of a rectangle formed by 130- and 031-type reflections from monoclinic VO_2 (see Fig. 3f). The presence of threefold rotations is due to VO_2 epitaxy on threefold crystal domain variants known to exist in pseudo-close-packed substrate surfaces such as mica [33–34]. The VO_2 (100) plane normals are aligned along the close-packed-direction of such substrates [35]. Thus, each grain in the polycrystalline films exhibits

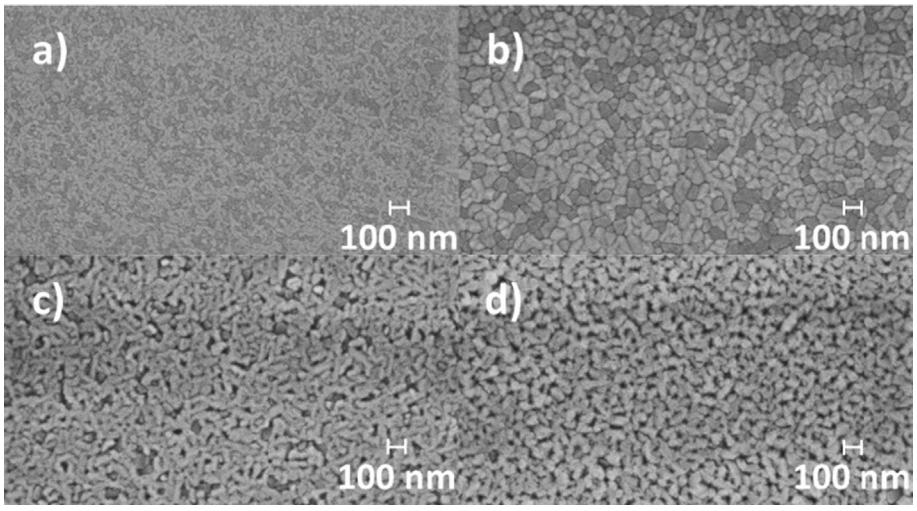

Fig. 1. Representative SEM micrographs from VO_2 films with thicknesses t_{film} = a) 17 nm, b) 26 nm, c) 61 nm, and d) 180 nm.

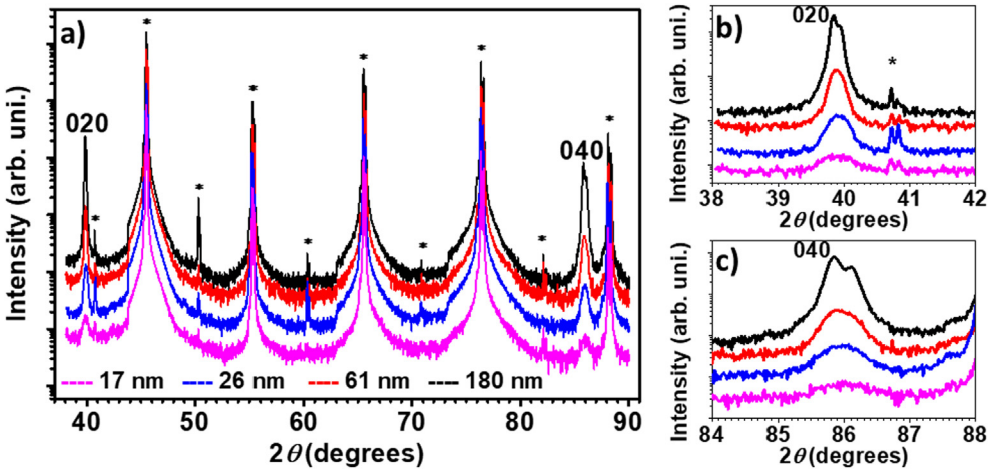

Fig. 2. a) X-ray diffractograms from VO_2 films with thicknesses in the 17 nm $\leq t_{film} \leq$ 180 nm range. Substrate peaks are indicated by "*". (b-c) magnifications of the 020 and 040 peaks.

an epitaxial relationship with the substrate, with three different possible in-plane domain orientations corresponding to the three in-plane orientational variants in the substrate.

High-resolution reciprocal space maps (RSMs) of the closely spaced 130-031 doublets and the 020 peaks (see Fig. 4) indicate that the VO_2 films are stress-free. From the 130/031 peak positions and assuming β = 122.6°, [32] we obtain a = 5.74 ± 0.02 nm, c = 5.35 ± 0.02 nm for 61 nm $\leq t_{film} \leq$ 180 nm. RSMs of 020 Bragg reflections yield b = 0.4526 ± 0.0004 nm for 17 nm $\leq t_{film} \leq$ 180 nm. These results corroborate the conclusions from Fig. 2 that the lattice parameters do not change with film thickness, with an order-of-magnitude greater precision, and confirm that all our films are stress-free.

The above results show in-plane as well as out-of-plane textures in stress-free VO_2 films, thus fulfilling the necessary conditions for VDWE. The large lattice mismatch between VO_2 and mica show that the film-substrate bonding is weak. As mentioned earlier, prior works claiming VDWE of VO_2 films demonstrated evidence for at most two of the three conditions, and in some cases assumed VDWE despite evidence to the contrary. It is important to note that the films are polycrystalline and epitaxial; each grain is epitaxially related to the substrate, with three different possible in-plane domain orientations.

Further analyses of the RSM peaks offer insights into the VDWE mechanism of VO_2 on mica. The elliptically shaped 020 peaks seen in films with $t_{film} \geq$ 26 nm indicate different in-plane and out-of-plane correlation lengths. In contrast, the 020 peak for t_{film} = 17 nm exhibits a narrow lateral width (|| to q_x) indicative of large in-plane crystal domain size, and out-of-plane streaks (|| to q_z) expected from small out-of-plane crystal dimensions. The in-plane correlation length $d_{ip} = 2\pi/\Delta q_x$ varies in the 10 $\leq d_{ip} \leq$ 15 nm range and exhibits a minimum at t_{film} = 26 nm (see Fig. 4h). In contrast, the out-of-plane correlation length $d_{op} = 2\pi/\Delta q_z$ monotonically increases with film thickness. The out-of-plane correlation lengths are 9 nm $\leq d_{op} \leq$ 38 nm, values 40–80% lower than the film thickness except for t_{film} = 26 nm, where d_{op} is similar to t_{film}. A similar lateral correlation length trend is obtained from the analyses of 130/031 asymmetric peaks [36] (see supplementary Fig. S6). Since $d_{op} > d_{ip}$, and d_{op} scales monotonically with t_{film}, our results indicate anisotropic growth of crystal domains. The initial decrease in d_{ip} suggests that large in-plane domains nucleate first, followed by further nucleation and growth influenced by factors other than the strong film-substrate bonding [37]. Upon further film growth, both d_{ip} and d_{op} increase. The increase of the latter at a higher rate is indicative of layer-by-layer growth of the basal planes within each crystal domain.

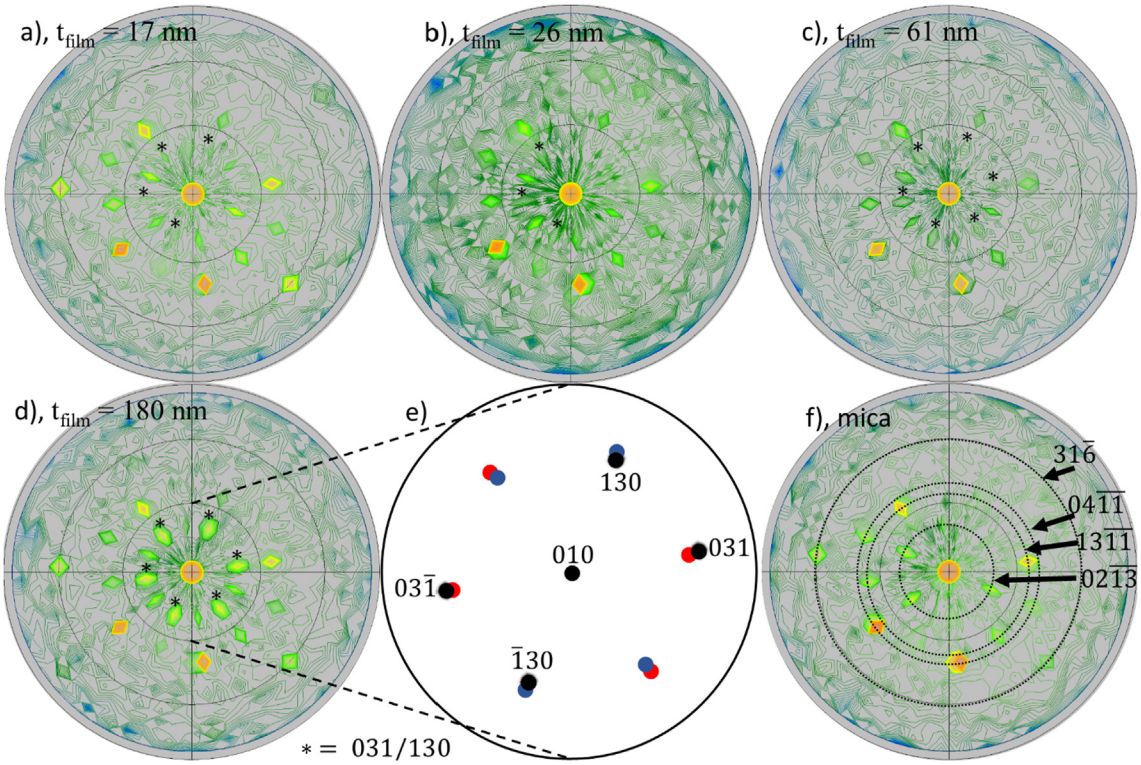

Fig. 3. Pole figures of the 031/130 VO_2 reflections on t_{film} = 17 nm in a), t_{film} = 26 nm in b), t_{film} = 62 nm in c), t_{film} = 180 nm in d) and bare substrate on f). e) is a magnified schematic pole figure of the 031/130 pole figures at three different in-plane orientations represented by red, blue, and black dots. (For interpretation of the references to colour in this figure legend, the reader is referred to the web version of this article.)

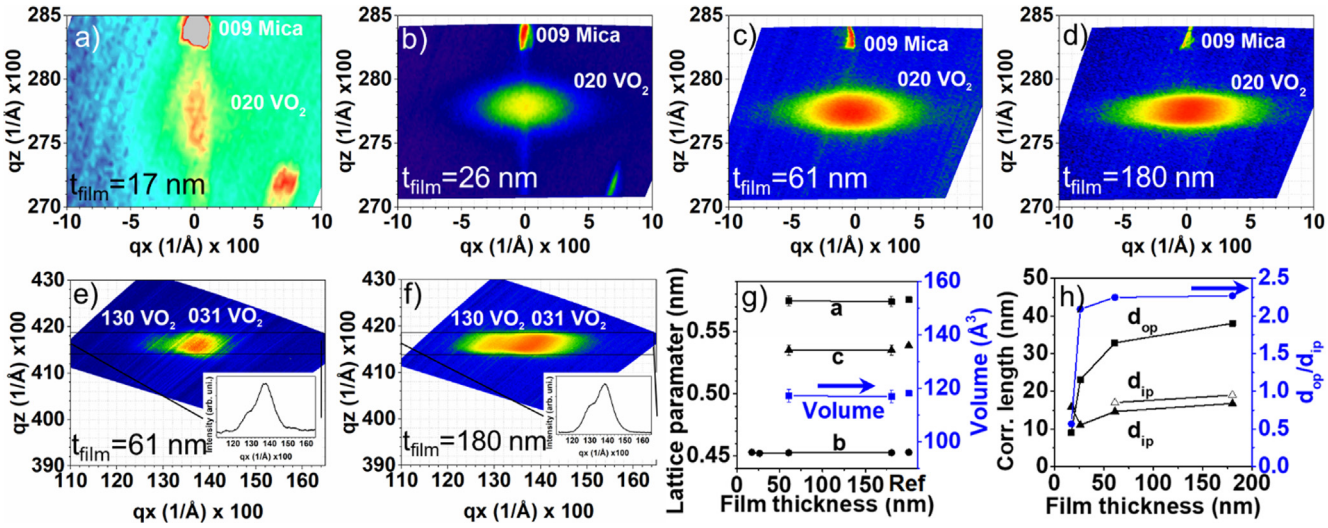

Fig. 4. Reciprocal space maps of the 020 (a-d) and 130/031 (e-f) reflections. Insets in e) and f) show line scans along q_x of the doublet peak. g) Lattice parameters and unit cell volume h) the correlation length evolution with thickness is shown in the black curves where squares, open triangles and triangles correspond to d_{op}, d_{ip}(from asymmetric RSM) and d_{ip}, respectively. The blue plot shows the relation of vertical over lateral correlation length. (For interpretation of the references to colour in this figure legend, the reader is referred to the web version of this article.)

Based on the above results, the VDWE of VO_2 and mica can be described by the orientation relationship VO_2 (010) || mica (001) and VO_2 [100] || mica [100] wherein the vanadium ions overlap approximately with every third Si atom on the mica substrate surface. Three epitaxial domains of VO_2 are observed because the mica substrate has three variant orientations.

Ab initio molecular dynamics (AIMD) simulations of up to 1.5-nm-sized VO_2 clusters allowed to relax for up to 4 ps reveal no preferred orientations on mica surfaces with or without potassium, likely due to sub-critical VO_2 cluster sizes. However, our results show the presence of potassium atoms in VO_2 clusters even at locations away from the VO_2-mica interface (Fig. 5a), suggesting that the surface potassium on mica actively participates in VO_2 nucleation. *Ab initio* density functional theory (DFT) calculations of single-crystal VO_2 layers on mica (Fig. 5b-c) reveal oxygen-ligation-induced out-of-plane polarization of electron clouds around some potassium atoms (Fig. 5d-g), pointing to the genesis of van der Waals-type weak bonding interactions that promote

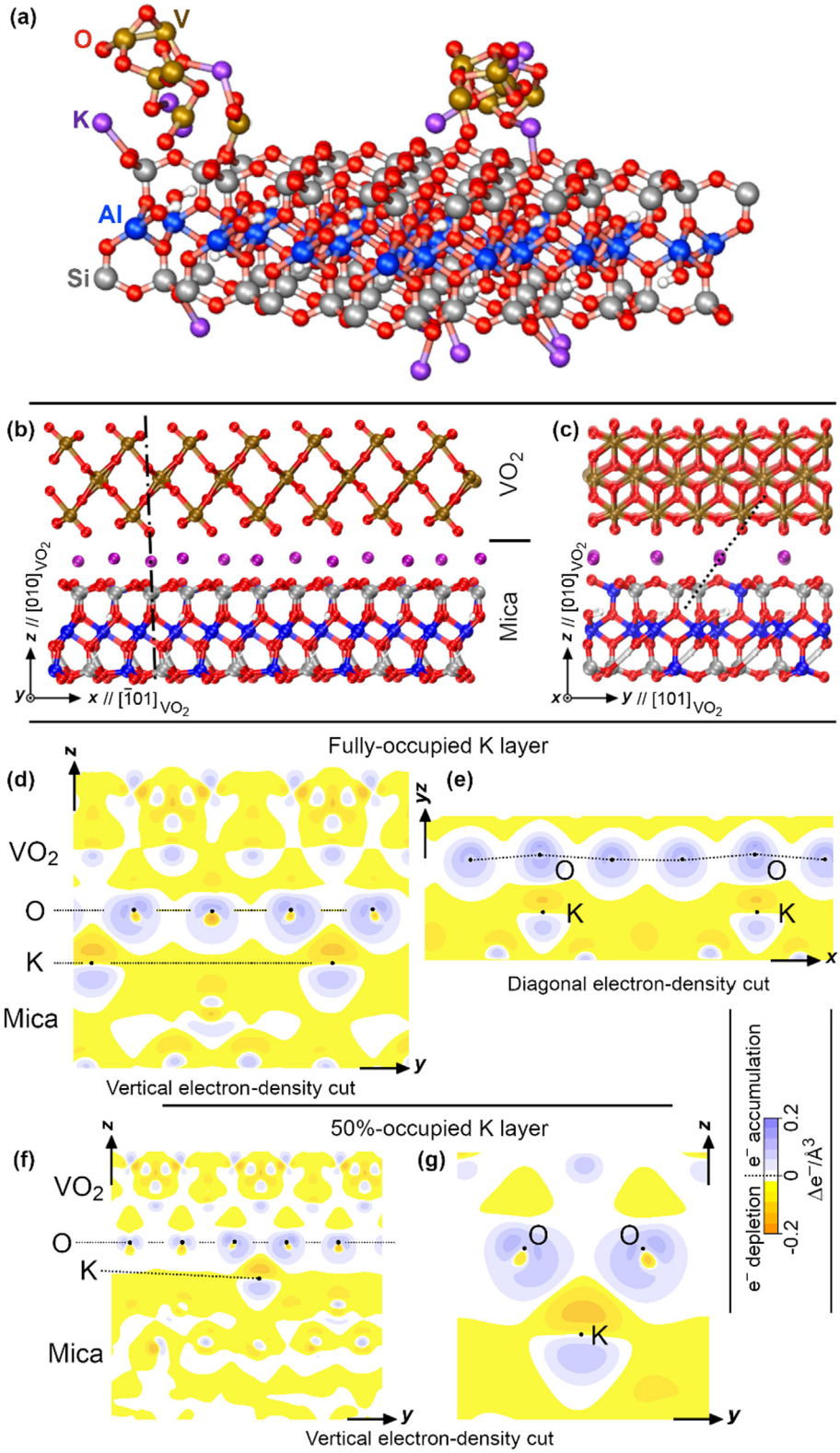

Fig. 5. (a) *Ab initio* molecular dynamics simulations capturing the presence of K in VO_2 nuclei formed on K-terminated mica, and (b,c) Schematic views of a DFT-relaxed VO_2-mica interface. Scheme: K-purple, Al-blue, Si-gray, H- white, O- red and V- brown. Electron-density transfer maps obtained by DFT calculations for the VO_2/mica interfaces with (d,e) 100% K and (f,g) 50% K. Dash-dot and diagonal dashed lines indicate planes used to visualize electron-transfer maps. (For interpretation of the references to colour in this figure legend, the reader is referred to the web version of this article.)

epitaxy. The nearly identical electron transfer at the K-O interface seen for mica surfaces with 50% and 100% potassium coverage suggest that the threshold potassium coverage for seeding VDWE may be even less than 50%. The electron cloud polarization symmetry correlates well with the experimentally observed epitaxial configuration of VO_2 on mica. For example, the electron-depleted lobes of

potassium atoms surrounded by oxygen electron-accumulation clouds on ($\bar{1}$01) planes along [101] directions (Fig. 5d) are consistent with the experimentally determined VO_2-mica orientation relationship. These electron deficient lobes near potassium hinder the glide of VO_2 crystals along the Cartesian abscissa and ordinate directions, and likely serve as anchor pins that foster epitaxial growth. These results underscore not only the subtle role of surface chemistry on seeding VDWE, but also the importance of *ab initio* calculations in uncovering such effects.

The phase transition is confirmed by both ellipsometry and XRD coupled with *in-situ* annealing as shown in supplementary Fig. S7 and S8 and the electrical conductivity is largely affected by the transition as shown in Fig. 6 where conductivity as a function of temperature is shown. The crystal domain correlation lengths in VO_2 films strongly correlate with the electrical conductivity hysteresis characteristics associated with the monoclinic-to-rutile insulator-to-metal transition [38–39] underpinned by the higher phase transition temperature during heating (T_H) than the reverse transition during cooling (T_C).

Two distinct conductivity regimes are observed: $20 \leq \sigma_{low} \leq 80$ S m^{-1} and $10^5 < \sigma_{high}$ less than 4 x10^5 S m^{-1} (see Fig. 6a-d), which is comparable to that reported previously [40]. The hysteresis loop-width decreases with increasing film thickness while transition sharpness is largely unaffected. Furthermore, T_H and transition width decrease linearly while T_C and σ_{low} increase as a function of d_{ip} and d_{op} for 26 nm $\leq t_{film} \leq$ 180 nm (see Fig. S9 in supplementary details). These observations are consistent with previously reported [41] crystal-size dependence on the phase transition temperature. By analyzing the electrical conductivity as a function of temperature using the Arrhenius plot, we find that the activation energy is in the $0.16 \leq E_a \leq 0.27$ eV range and decreases with increasing thickness. These values are close to the 0.3 eV reported for low-defect films [42–43] (see supplementary Fig. S10).

The hysteresis characteristics depend on many factors such as stress and doping, neither of which have contributions in our stress-free VDWE VO_2 films. For example, film stress has been shown to either increase or decrease T_C and T_H [44–45], while defects and grain size influence in nucleating the phase transition. [46–47] In this work, we hypothesize that the coherent domain size in the crystal structure is an important factor on the phase transition hysteresis shape. As the in-plane and out-of-plane correlation lengths has been shown to affect the transition temperature and hysteresis width where longer correlation lengths reduced the hysteresis width. [41,48] However, there are other studies that report opposite behavior of T_C and T_H with crystal size (correlation length), highlighting the complexity of the hysteresis. [49].

4. Conclusions

Epitaxial VO_2 films were grown on mica substrates using reactive pulsed magnetron sputtering. The films were stress-free and exhibited both in-plane and out-of-plane textures, showing van der Waals epitaxy. We note that without the presence of all these three parameters, VDWE cannot be inferred with certainty. *Ab initio* calculations show that surface potassium atoms in mica provides a mechanism for epitaxy with weak film-substate bonding. Our observations highlight the problem in the literature where VDWE is often simply assumed based on the chosen material systems, with insufficient evidence for all three factors or incorrectly inferred based merely on the assumptions on the stress-state and/or nature of the film-substrate bonding. Analyses of diffraction patterns indicate that the nucleation of large in-plane domains supports the subsequent growth of islands. The film thickness, and the epitaxial domain sizes in the films are controllable by adjusting the deposition time without any interfacial stress generation. Combining the changes in correlation length and stress-free films, a linear relation between the shape of the hysteresis and correlation length is observed in the 26 nm to 180 nm film thickness range.

Declaration of Competing Interest

The authors declare that they have no known competing financial interests or personal relationships that could have appeared to influence the work reported in this paper.

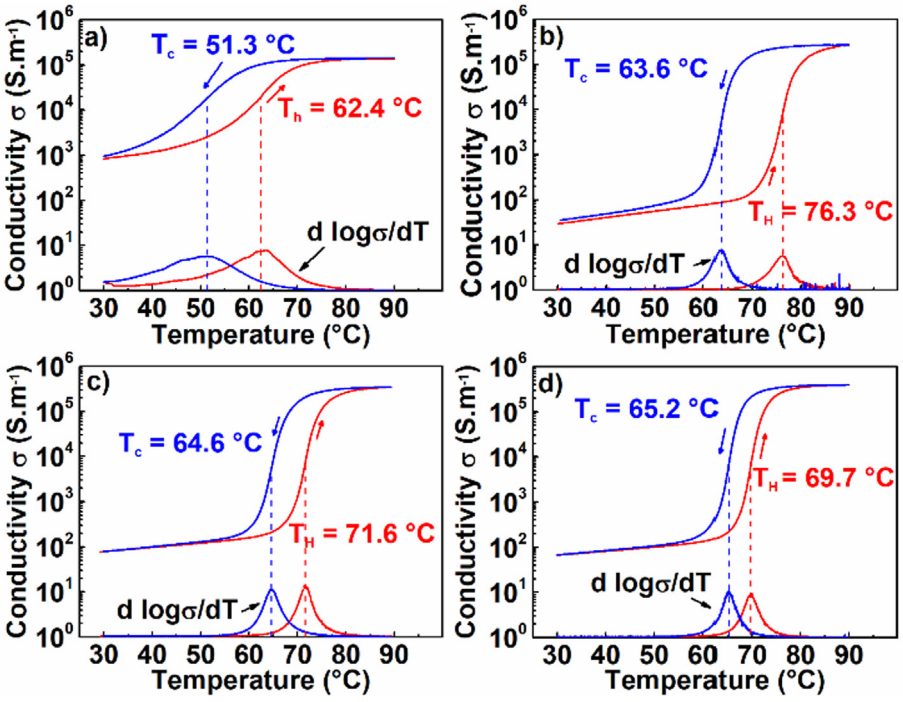

Fig. 6. Electrical conductivity versus temperature for different film thicknesses of t_{film} = a) 17 nm, b) 26 nm, c) 61 nm, and d) 180 nm.

Acknowledgments

The work was supported by the Swedish Government Strategic Research Area in Materials Science on Functional Materials at Linköping University (Faculty Grant SFO-Mat-LiU No. 2009 00971), the Swedish Research Council (project numbers 2021-03826 and 2021-04426), the Swedish Energy Agency (project number 46519-1) the Knut and Alice Wallenberg foundation through the Wallenberg Academy Fellows program (KAW-2020.0196), the Linköping Electron Microscopy Laboratory, and the Swedish Foundation for Strategic Research (SSF) under the Research Infrastructure Fellow RIF 14-0074 program. S. H. acknowledges the French government program "Investissements d'Avenir" (EUR INTREE, reference ANR-18-EURE-0010, and LABEX INTERACTIFS, reference ANR-11-LABX-0017-01). G.R. and G.S. gratefully acknowledge funding from the US National Science Foundation through grant CMMI 2135725. DFT calculations were carried out using the resources provided by the Swedish National Infrastructure for Computing (SNIC) - partially funded by the Swedish Research Council through Grant Agreement Nº VR-2018-05973.

Author contributions

E.E., B.P., F. E., A. l. F., and P.E conceived and initiated the study. F.E., B. P. G. R. and P. E. supervised the research.

E.E. planned and performed all thin-film growth and characterization by XRD and SEM with input from F.E., A. l. F., B.P, G. R. and P. E.

S. H. performed and analyzed the ellipsometry and electrical characterization with input from E.E and A. l. F.

A. E. and P.O.Å.P performed and analyzed the TEM characterization.

G.S., O. V, and D.G.S performed the *ab initio* studies and wrote the corresponding parts of the manuscript.

E.E., G. R. and P.E wrote the manuscript with contributions from all the co-authors.

All co-authors read, edited, and commented on successive version of the manuscript.

Data availability

The data that support these findings are available from the corresponding authors on request.

Appendix A. Supplementary data

Supplementary data to this article can be found online at https://doi.org/10.1016/j.matdes.2023.111864.

References

[1] H. Brune, Microscopic view of epitaxial metal growth: nucleation and aggregation, Surf. Sci. Rep. 31 (1998) 121–229.
[2] A. Koma, Van der Waals epitaxy—a new epitaxial growth method for a highly lattice-mismatched system, Thin Solid Films 216 (1992) 72–76, https://doi.org/10.1016/0040-6090(92)90872-9.
[3] S. Steinberg et al., Van der Waals Epitaxial Growth of α-Alumina Nanocrystals on Mica, Science 260 (1993) 656–659, https://doi.org/10.1126/science.260.5108.656.
[4] A. Klein, W. Jaegermann, Review—Electronic Properties of 2D Layered Chalcogenide Surfaces and Interfaces grown by (quasi) van der Waals Epitaxy, ECS J. Solid State Sci. Technol. 9 (2020), https://doi.org/10.1149/2162-8777/abb750 093012.
[5] Y. Bitla, Y.H. Chu, MICAtronics: A new platform for flexible X-tronics, Flatchem 3 (2017) 26–42, https://doi.org/10.1016/j.flatc.2017.06.003.
[6] S.H. Bae et al., Integration of bulk materials with two-dimensional materials for physical coupling and applications, Nat. Mater. 18 (2019) 550–560, https://doi.org/10.1038/s41563-019-0335-2.
[7] A. Koma, Molecular-Beam Epitaxial-Growth of Organic Thin-Films, Prog. Cryst. Growth Charact. Mater. 30 (1995) 129-152, Doi: 10.1016/0960-8974(95)00009-V.
[8] A.K. Geim, I.V. Grigorieva, van der Waals heterostructures, Nature 499 (2013) 419–425, https://doi.org/10.1038/nature12385.
[9] M. Kratzer, A. Matkovic, C. Teichert, Adsorption and epitaxial growth of small organic semiconductors on hexagonal boron nitride, J. Phys. D-Appl. Phys. 52 (2019) 23, doi:10.1088/1361-6463/ab29cb.
[10] S.Z. Butler et al., Progress, challenges, and opportunities in two-dimensional materials beyond graphene, ACS Nano 7 (2013) 2898–2926, https://doi.org/10.1021/nn400280c.
[11] G.R. Bhimanapati et al., Recent Advances in Two-Dimensional Materials beyond Graphene, ACS Nano 9 (2015) 11509–11539, https://doi.org/10.1021/acsnano.5b05556.
[12] Z.M. Wei et al., Various Structures of 2D Transition-Metal Dichalcogenides and Their Applications, Small Methods 2 (2018) 19, doi: 10.1002/smtd.201800094.
[13] Q. Chen et al., Van der Waals Epitaxy of III-Nitrides and Its Applications, Materials (Basel) 13 (2020) 17, https://doi.org/10.3390/ma13173835.
[14] Y.H. Chu, Van der Waals oxide heteroepitaxy. Npj Quantum Materials 2 (2017) 67. doi: 6710.1038/s41535-017-0069-9.
[15] P.A. Vermeulen, J. Mulder, J. Momand, B.J. Kooi, Strain engineering of van der Waals heterostructures, Nanoscale 10 (2018) 1474–1480, https://doi.org/10.1039/C7NR07607J.
[16] Z.W. Shao et al., Controllable phase-transition temperature upon strain release in VO_2/MgF_2 epitaxial films, J. Appl. Phys. 128 (2020) 045303. doi:Artn 04530310.1063/5.0011423.
[17] X. Cheng et al., Enhanced Phase Transition Properties of VO2 Thin Films on 6H-SiC (0001) Substrate Prepared by Pulsed Laser Deposition, Nanomaterials (Basel, Switzerland) 9 (2019), doi:10.3390/nano9081061.
[18] S. Kittiwatanakul, S.A. Wolf, J.W. Lu, Large epitaxial bi-axial strain induces a Mott-like phase transition in VO_2, Appl. Phys. Lett. 105 (2014) 073112, doi: Artn 07311210.1063/1.4893326.
[19] F.J. Morin, Oxides Which Show a Metal-to-Insulator Transition at the Neel Temperature, Phys. Rev. Lett. 3 (1959) 34–36, https://doi.org/10.1103/PhysRevLett.3.34.
[20] J.B. Goodenough, The two components of the crystallographic transition in VO_2, J. Solid State Chem. 3 (1971) 490–500, https://doi.org/10.1016/0022-4596(71)90091-0.
[21] B. Yan, F. Hao, X. Meng, When artificial intelligence meets building energy efficiency, a review focusing on zero energy building, Artif. Intell. Rev. 54 (2021) 2193–2220, https://doi.org/10.1007/s10462-020-09902-w.
[22] M. Aburas et al., Thermochromic smart window technologies for building application: A review, Appl. Energy 255 (2019)113522, https://doi.org/10.1016/j.apenergy.2019.113522.
[23] Y.Y. Cui et al., Thermochromic VO_2 for Energy-Efficient Smart Windows, Joule 2 (2018) 1707–1746, https://doi.org/10.1016/j.joule.2018.06.018.
[24] C.G. Granqvist, Transparent conductors as solar energy materials: A panoramic review, Sol. Energy Mater. Sol. Cells 91 (2007) 1529–1598, https://doi.org/10.1016/j.solmat.2007.04.031.
[25] W.Z. Liang, et al., Van der Waals Heteroepitaxial VO_2/Mica Films with Extremely Low Optical Trigger Threshold and Large THz Field Modulation Depth. Advanced Optical Materials 7 (2019) 1900647, doi: ARTN 1900647 10.1002/adom.201900647.
[26] Z. Yang, C.Y. Ko, S. Ramanathan, Oxide Electronics Utilizing Ultrafast Metal-Insulator Transitions, Annu. Rev. Mat. Res. 41 (41) (2011) 337–367, https://doi.org/10.1146/annurev-matsci-062910-100347.
[27] C. Zou, J.J. Zheng, C. Chang, A. Majumdar, L.Y. Lin, Nonvolatile Rewritable Photomemory Arrays Based on Reversible Phase-Change Perovskite for Optical Information Storage, Adv. Opt. Mater. 7 (2019) 1900558, https://doi.org/10.1002/adom.201900558.
[28] Q.J. Lu et al., Role of seed layer in van der Waals growth of vanadium dioxide film on mica prepared by chemical solution deposition, J. Sol-Gel Sci. Technol. 98 (2021) 24–30, https://doi.org/10.1007/s10971-021-05478-1.
[29] C.I. Li et al., van der Waal Epitaxy of Flexible and Transparent VO_2 Film on Muscovite, Chem. Mater. 28 (2016) 3914–3919, https://doi.org/10.1021/acs.chemmater.6b01180.
[30] Y.-X. Liu et al., Van der Waals epitaxy for high-quality flexible VO_2 film on mica substrate, J. Appl. Phys. 130 (2021), https://doi.org/10.1063/5.0046827 025301.
[31] S. Pendse et al., Tuning phase transition kinetics via van der Waals epitaxy of single crystalline VO_2 on hexagonal-BN, J. Cryst. Growth 543 (2020) 125699, https://doi.org/10.1016/j.jcrysgro.2020.125699.
[32] VO2 Crystal Structure: Datasheet from "PAULING FILE Multinaries Edition – 2012" in SpringerMaterials (https://materials.springer.com/isp/crystallographic/docs/sd_0455502) (Springer-Verlag Berlin Heidelberg & Material Phases Data System (MPDS), Switzerland & National Institute for Materials Science (NIMS), Japan).
[33] Y. Bitla et al., Oxide Heteroepitaxy for Flexible Optoelectronics, ACS Appl. Mater. Interfaces 8 (2016) 32401–32407, https://doi.org/10.1021/acsami.6b10631.
[34] C.H. Ma et al., Van der Waals epitaxy of functional MoO_2 film on mica for flexible electronics, Appl. Phys. Lett. 108 (2016) 253104, https://doi.org/10.1063/1.4954172.
[35] F.J. Wong, Y. Zhou, S. Ramanathan, Epitaxial variants of VO_2 thin films on complex oxide single crystal substrates with 3m surface symmetry, J. Cryst. Growth 364 (2013) 74–80, https://doi.org/10.1016/j.jcrysgro.2012.11.054.

[36] P.F. Fewster, X-ray Scattering From Semiconductors, second ed., World Scientific Publishing Company, 2003.
[37] R.Y. Yue et al., Nucleation and growth of WSe_2: enabling large grain transition metal dichalcogenides. 2D Mater. 4 (2017) 10. https://doi.org/10.1088/2053-1583/aa8ab5.
[38] A. Cavalleri et al., Femtosecond Structural Dynamics in VO_2 during an Ultrafast Solid-Solid Phase Transition, Phys. Rev. Lett. 87 (2001), https://doi.org/10.1103/PhysRevLett.87.237401 237401.
[39] M.M. Qazilbash et al., Mott transition in VO_2 revealed by infrared spectroscopy and nano-imaging, Science 318 (2007) 1750–1753, https://doi.org/10.1126/science.1150124.
[40] H.T. Zhang et al., Wafer-scale growth of VO_2 thin films using a combinatorial approach, Nat. Commun. 6 (2015) 8475, https://doi.org/10.1038/ncomms9475.
[41] R. Lopez, T.E. Haynes, L.A. Boatner, L.C. Feldman, R.F. Haglund, Size effects in the structural phase transition of VO_2 nanoparticles, Phys. Rev. B 65 (2002) 5, https://doi.org/10.1103/PhysRevB.65.224113.
[42] J.C. Orlianges et al., Electrical and optical properties of vanadium dioxide containing gold nanoparticles deposited by pulsed laser deposition, Appl. Phys. Lett. 101 (2012) 133102, doi: Artn 133102 10.1063/1.4754708.
[43] J. Wei, Z. Wang, W. Chen, D.H. Cobden, New aspects of the metal-insulator transition in single-domain vanadium dioxide nanobeams, Nat. Nanotechnol. 4 (2009) 420–424, https://doi.org/10.1038/nnano.2009.141.
[44] Y. Cui, S. Shi, L. Chen, H. Luo, Y. Gao, Hydrogen-doping induced reduction in the phase transition temperature of VO_2: a first-principles study, Phys. Chem. Chem. Phys. 17 (2015) 20998–21004, https://doi.org/10.1039/c5cp03267a.
[45] H.W. Chen, C.I. Li, C.H. Ma, Y.H. Chu, H.L. Liu, Strain engineering of optical properties in transparent VO_2/muscovite heterostructures, Phys. Chem. Chem. Phys. 23 (2021) 8908–8915, https://doi.org/10.1039/d1cp00642h.
[46] W. Fan et al., Large kinetic asymmetry in the metal-insulator transition nucleated at localized and extended defects, Phys. Rev. B 83 (2011) 235102, https://doi.org/10.1103/PhysRevB.83.235102.
[47] L.T. Kang et al., Effects of Annealing Parameters on Optical Properties of Thermochromic VO_2 Films Prepared in Aqueous Solution, J. Phys. Chem. C 114 (2010) 1901–1911, https://doi.org/10.1021/jp909009w.
[48] R.A. Aliev et al., Effect of grain sizes on the metal-semiconductor phase transition in vanadium dioxide polycrystalline thin films, Phys. Solid State 48 (2006) 929–934, https://doi.org/10.1134/S1063783406050180.
[49] M. Wang, Y.Q. Xue, Z.X. Cui, R. Zhang, Size-Dependent Crystal Transition Thermodynamics of Nano-VO_2 (M), J. Phys. Chem. C 122 (2018) 8621–8627, https://doi.org/10.1021/acs.jpcc.8b01183.
[50] A. le Febvrier et al., An upgraded ultra-high vacuum magnetron-sputtering system for high-versatility and software-controlled deposition, Vacuum 187 (2021), https://doi.org/10.1016/j.vacuum.2021.110137 110137.
[51] J. VandeVondele et al., QUICKSTEP: Fast and accurate density functional calculations using a mixed Gaussian and plane waves approach, Comput. Phys. Commun. 167 (2005) 103–128, https://doi.org/10.1016/j.cpc.2004.12.014.
[52] J. VandeVondele, J. Hutter, Gaussian basis sets for accurate calculations on molecular systems in gas and condensed phases, J. Chem. Phys. 127 (2007), https://doi.org/10.1063/1.2770708.
[53] S. Goedecker, M. Teter, J. Hutter, Separable dual-space Gaussian pseudopotentials, Phys. Rev. B 54 (1996) 1703–1710, https://doi.org/10.1103/PhysRevB.54.1703.
[54] J.P. Perdew, K. Burke, M. Ernzerhof, Generalized gradient approximation made simple, Phys. Rev. Lett. 77 (1996) 3865–3868, https://doi.org/10.1103/PhysRevLett.77.3865.
[55] G. Kresse, D. Joubert, From ultrasoft pseudopotentials to the projector augmented-wave method, Phys. Rev. B 59 (1999) 1758–1775, https://doi.org/10.1103/PhysRevB.59.1758.
[56] I. van der Hamada, Waals density functional made accurate, Phys. Rev. B 89 (2014), https://doi.org/10.1103/PhysRevB.89.121103.
[57] A.I. Liechtenstein, V.I. Anisimov, J. Zaanen, DENSITY-FUNCTIONAL THEORY AND STRONG-INTERACTIONS - ORBITAL ORDERING IN MOTT-HUBBARD INSULATORS, Phys. Rev. B 52 (1995) R5467–R5470, https://doi.org/10.1103/PhysRevB.52.R5467.